The Astronomical Journal, 167:165 (15pp), 2024 April https://doi.org/10.3847/1538-3881/ad26ff

An ALMA Molecular Inventory of Warm Herbig Ae Disks. II. Abundant Complex Organics and Volatile Sulphur in the IRS 48 Disk

Alice S. Booth[1,2,12], Milou Temmink[1], Ewine F. van Dishoeck[1,3], Lucy Evans[4], John D. Ilee[4], Mihkel Kama[5,6], Luke Keyte[5], Charles J. Law[7,13], Margot Leemker[1], Nienke van der Marel[1], Hideko Nomura[8], Shota Notsu[9,10,11], Karin Öberg[2], and Catherine Walsh[4]
[1] Leiden Observatory, Leiden University, 2300 RA Leiden, The Netherlands; alice.booth@cfa.harvard.edu
[2] Center for Astrophysics | Harvard & Smithsonian, 60 Garden Street, Cambridge, MA 02138, USA
[3] Max-Planck-Institut für Extraterrestrische Physik, Giessenbachstrasse 1, 85748 Garching, Germany
[4] School of Physics and Astronomy, University of Leeds, Leeds LS2 9JT, UK
[5] Department of Physics and Astronomy, University College London, Gower Street, London, WC1E 6BT, UK
[6] Tartu Observatory, University of Tartu, Observatooriumi 1, 61602 Tõravere, Tartumaa, Estonia
[7] Department of Astronomy, University of Virginia, Charlottesville, VA 22904, USA
[8] Division of Science, National Astronomical Observatory of Japan, 2-21-1 Osawa, Mitaka, Tokyo 181-8588, Japan
[9] Department of Earth and Planetary Science, Graduate School of Science, The University of Tokyo, 7-3-1 Hongo, Bunkyo-ku, Tokyo 113-0033, Japan
[10] Department of Astronomy, Graduate School of Science, The University of Tokyo, 7-3-1 Hongo, Bunkyo-ku, Tokyo 113-0033, Japan
[11] Star and Planet Formation Laboratory, RIKEN Cluster for Pioneering Research, 2-1 Hirosawa, Wako, Saitama 351-0198, Japan
Received 2023 November 21; revised 2024 January 19; accepted 2024 January 31; published 2024 March 18

Abstract

The Atacama Large Millimeter/submillimeter Array (ALMA) can probe the molecular content of planet-forming disks with unprecedented sensitivity. These observations allow us to build up an inventory of the volatiles available for forming planets and comets. Herbig Ae transition disks are fruitful targets due to the thermal sublimation of complex organic molecules (COMs) and likely H_2O-rich ices in these disks. The IRS 48 disk shows a particularly rich chemistry that can be directly linked to its asymmetric dust trap. Here, we present ALMA observations of the IRS 48 disk where we detect 16 different molecules and make the first robust detections of $H_2^{13}CO$, ^{34}SO, ^{33}SO, and c-H_2COCH_2 (ethylene oxide) in a protoplanetary disk. All of the molecular emissions, aside from CO, are co-located with the dust trap, and this includes newly detected simple molecules such as HCO^+, HCN, and CS. Interestingly, there are spatial offsets between different molecular families, including between the COMs and sulfur-bearing species, with the latter being more azimuthally extended and radially located further from the star. The abundances of the newly detected COMs relative to CH_3OH are higher than the expected protostellar ratios, which implies some degree of chemical processing of the inherited ices during the disk lifetime. These data highlight IRS 48 as a unique astrochemical laboratory to unravel the full volatile reservoir at the epoch of planet and comet formation and the role of the disk in (re)setting chemical complexity.

Unified Astronomy Thesaurus concepts: Planet formation (1241); Complex organic molecules (2256); Interferometry (808); Chemical abundances (224); Astrochemistry (75)

1. Introduction

Due to the sensitivity of the Atacama Large Millimeter/submillimeter Array (ALMA), we now have unmatched access to the volatile reservoir in planet-forming disks. In recent years, ALMA has enabled the detection of both new disk molecules including SO_2 and CH_3CN, and rare isotopologues (e.g., $^{13}C^{17}O$ and $HC^{18}O^+$; Öberg et al. 2015; Booth et al. 2019, 2021a; Furuya et al. 2022). What is particularly exciting is the detection of complex organic molecules (COMs), which are defined as molecules containing at least six atoms and of which at least one is carbon (Herbst & van Dishoeck 2009). Although the first detection of the simplest COM CH_3OH in a Class II T-Tauri disk (TW Hya) traced a very low abundance of cold CH_3OH (Walsh et al. 2016), subsequent observations of warmer Herbig Ae transition disks have revealed abundant thermally desorbed CH_3OH and even other COMs of higher complexity (van der Marel et al. 2021a; Booth et al. 2021b; Brunken et al. 2022; Booth et al. 2023). The detection of abundant COMs in warm Herbig Ae disks is clear evidence for the inheritance of ices from the earlier stages of star formation. This is because CH_3OH only forms efficiently on the surfaces of cold dust grains and primarily via the hydrogenation of CO ice (Watanabe & Kouchi 2002; Fuchs et al. 2009; Santos et al. 2022).

In the warm young F/Herbig Ae disks HD 100546, IRS 48, and HD 169142 there is no evidence of significant CO freeze-out, meaning that the observed reservoir of CH_3OH cannot have formed in situ. This was shown directly for the HD 100546 disk using astrochemical models (Booth et al. 2021b). Therefore, in order for CH_3OH to be present in these systems, CH_3OH-rich ices must survive the star formation process and be transported to the inner disk where they thermally sublimate. CH_3OH will come off the grains at a similar temperature as H_2O (Minissale et al. 2022) and therefore the bulk of the volatile content of the disks should also be in the gas phase in this region of the disk. These sources therefore give us a window into a typically unobservable molecular reservoir in disks.

[12] Clay Postdoctoral Fellow.
[13] NASA Hubble Fellowship Program Sagan Fellow.

Table 1
Properties of the IRS 48 and HD 100546 Star and Disk Systems

Source	Type	Dist. (pc)	Incl. (deg)	PA (deg)	L ($L_\odot$)	M_* ($M_\odot$)	$M_{\rm dust}$ ($M_\odot$)	$M_{\rm gas}$ ($M_\odot$)	log $_{10}(\dot{M}_{\rm acc})$ ($M_\odot$ yr^{-1})	log10($L_{\rm Xray}$) (erg s^{-1})	$v_{\rm sys}$ (km s^{-1})	References
IRS 48	A0	135	50.0	100.0	14.3	2.0	1.5×10^{-5}	5.5×10^{-4}	−8.40	<27.0	4.55	[1-7]
HD 100546	A0-A1	110	41.7	146.0	23.5	2.2	1.1×10^{-3}	1.5×10^{-1}	−6.81	28.1	5.70	[8-13]

Note. References: [1] Brown et al. (2012), [2] Follette et al. (2015), [3] Gaia Collaboration et al. (2018), [4] Bruderer et al. (2014), [5] van der Marel et al. (2016), [6] Salyk et al. (2013), [7] Leemker et al. (2023), [8] Vioque et al. (2018) , [9] Guzmán-Díaz et al. (2021), [10] Walsh et al. (2014b), [11] Walsh et al. (2017), [12] Kama et al. (2016), [13] Meeus et al. (2012).

The disk most rich in COMs and potentially H_2O-derived volatiles like SO is the disk around the young star IRS 48. The IRS 48 disk has been well studied with ALMA and hosts the most asymmetric dust trap yet discovered at a distance of 60 au from the central star (van der Marel et al. 2013, 2021b; Yang et al. 2023). Its gas mass of only 5.5×10^{-4} $M_\odot$ is much lower than those of other Herbig Ae disks; yet it is very line rich, with detections of the CO isotopologues ^{12}CO, ^{13}CO, $C^{18}O$, $C^{17}O$ along with SO, SO_2, $^{34}SO_2$, NO, H_2CO, CH_3OH, CH_3OCH_3, and tentatively CH_3OCHO (van der Marel et al. 2013; Booth et al. 2021a; van der Marel et al. 2021a; Brunken et al. 2022; Leemker et al. 2023). The significance of the reported nondetections of CS, C_2H, and CN in IRS 48 was quantified by Booth et al. (2021a) and Leemker et al. (2023) and indicates a C/O ratio in the disk gas that is significantly less than 1. This low C/O and lack of C_2H is consistent with H_2O being in the gas phase and a general lack of volatile depletion at least at the location of the dust trap (Leemker et al. 2023).

There are several key simple molecules that have yet to be targeted in the IRS 48 disk, which would allow for a more complete comparison to other Herbig Ae disks. Here we present the results of an ALMA line survey of the IRS 48 disk, where we target >20 molecular species. These data provide key constraints on the abundances of HCO +, HCN, CN, C_2H, and CS in this system. Additionally, we further unravel the volatile sulfur and complex organic reservoir of the disk and discuss the physical/chemical origin of the molecular substructures observed. We particularly make a direct comparison between the molecular inventory of the IRS 48 and HD 100546 disks, where the initial results for the latter are presented in Booth et al. (2024), and contextualize the detections of COMs in these systems with protostellar environments.

2. Observations

IRS 48 was observed in the ALMA program 2021.1.00738.S (PI. A. S. Booth), and the general properties of the IRS 48 system are listed in Table 1. The data consist of two spectral settings with four spectral windows each at a spectral resolution of 976.6 kHz (0.84 km s^{-1} at 350 GHz) and a bandwidth of 1.875 GHz. These spectral windows are centered at 338.790824, 340.732413, 348.916936, and 350.775389 GHz for setting A and 344.240980, 3459.40999, 354.367095, and 356.067114 GHz for setting B. Further details on the individual execution blocks are provided in Table 4 of the Appendix; for full details of the data reduction, observational setup, and imaging please refer to the companion paper, which also presents data on the HD 100546 system (Booth et al. 2024). The self-calibration was performed on the IRS 48 continuum data after flagging the strong lines, which resulted in a continuum signal-to-noise ratio increase from ≈475 to ≈3220. This process consisted of four rounds of phase calibration and one round of amplitude calibration and resulted in the detection of the weak millimeter emission in the north of the IRS 48 disk. The data were imaged in CASA using `tCLEAN` with the multiscale deconvolver with a uniform velocity resolution of 0.9 km s^{-1}. These ≈0$''$3 data have a beam area 2.5× smaller than that presented in the series of papers from Booth et al. (2021a), van der Marel et al. (2021a), Brunken et al. (2022), and Leemker et al. (2023). Individual lines were cleaned with Keplerian masks down to 4× the rms of the dirty image where the Keplerian masks were constructed using the properties for the IRS 48 disk, as listed in Table 1. The properties of the transitions imaged and the resulting beam sizes and rms noise for each line are listed in Tables 5 and 6 of the Appendix.

3. Results

3.1. Molecules Detected

We use matched filtering to make an initial line identification (Loomis et al. 2018b). This technique uses the predictable Keplerian rotation of the disk gas to detect molecular lines in the visibility data via cross correlation of the UV data with a filter. This filter can be a smooth model, e.g., a Keplerian mask, the FITS output of a line radiative transfer model, or a strong line detection in the disk. In Figure 1 we present the resulting matched filter response over the full data set for the IRS 48 disk with a Keplerian model with an outer radius of 150 au compared to the HD 100546 response (outer radius of 300 au) that is presented in Booth et al. (2024). HD 100546 was observed in the same manner as IRS 48, and we find that the IRS 48 disk is more line rich, but there are different molecules detected in each disk. These differences may be attributed to different physical properties of the systems and/or the dominant chemical processes. Both are disks around young A-type stars, and the characteristics of these two systems are compared in Table 1. In Section 4.2 we discuss the similarities and differences both physical and chemical between the two disks. The fully annotated version of the IRS 48 filter response is shown in Figure 7 of the Appendix. From this, we have detected 16 molecular species in the IRS 48 disk where detection is defined as a matched filter response of at least 4σ. This includes robust detections of the rare isotopologues $H_2^{13}CO$, ^{34}SO, and ^{33}SO and the detection of the first heterocycle–ethylene oxide (c-H_2COCH_2)—in protoplanetary disks. We detect two lines of c-H_2COCH_2 with the fiducial Keplerian model filter at rest frequencies of 338.7720826 GHz and 350.3036524 GHz. Using alternative image filters does not yield a significant improvement in the detection strength—likely due to the compact nature of the emission. In the channel maps compact emission from c-H_2COCH_2 is detected at the 4σ level over the three consecutive channels where the CH_3OH lines are the strongest for both lines. Interestingly, although the

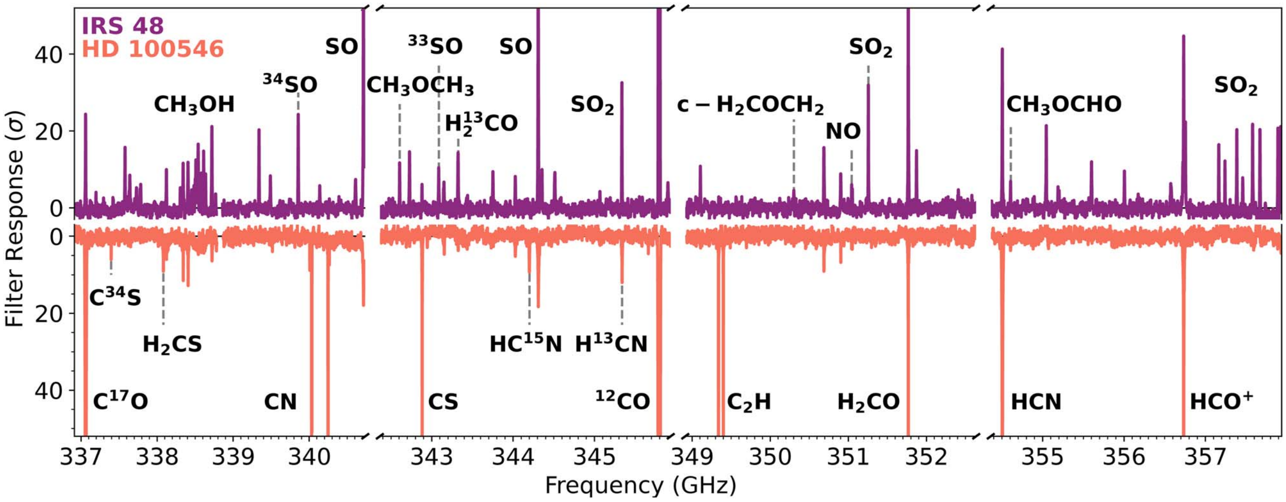

Figure 1. Matched filter responses for the IRS 48 and HD 100546 (taken from Booth et al. 2024) disks showing the full frequency coverage of the observations and highlighting the main molecules detected in each disk. Note that the HD 100546 response has been inverted, and the lines reaching the top and bottom of the *y*-axis have responses $>50\sigma$. The molecule labels at the top and bottom of the plot indicate from which disk the line is more strongly detected, and the vertical gray lines show the location of particular molecular transitions in more crowded regions of the spectrum. Both matched filter responses were generated using Keplerian models with an outer radius of 150 au for IRS 48 and 300 au for HD 100546. A fully annotated version of the IRS 48 response is shown in Figure 7.

isomer acetaldehyde (CH_3CHO) is typically more abundant (Ikeda et al. 2001; Lykke et al. 2017), it is not detected in the IRS 48 disk. Dimethyl ether (CH_3OCH_3) is detected again, as reported by Brunken et al. (2022), and their weak detection of methyl formate (CH_3OCHO) is clearly confirmed in our data. An investigation into other COMs lines covered in these data and upper limits on other nondetections will follow in K. Kipfer et al. (2024, in preparation). A summary of the molecules detected/nondetected in both the IRS 48 and HD 100546 disks is shown in Table 2. It is unclear from visual inspection of the data if $H^{13}CN$ is detected in IRS 48 or not as this line is blended with a strong SO_2 line. Using matched filtering and the HCN as a mask we find that $HC^{15}N$, CN, and C_2H are all not detected.

3.2. Integrated Intensity Maps

Figure 2 presents the 0.9 mm continuum map and the integrated intensity maps of the representative transitions of each molecule detected in the IRS 48 disk. This galley does not include the isotopologues of SO, which will be the focus of future work. These line maps were generated using the Keplerian masks generated in the CLEANing with no clipping thresholds. All of the molecules aside from ^{12}CO and $C^{17}O$ only show significant emission in the south of the disk—the same region of the disk as the millimeter dust trap. In the north of the disk, the ^{12}CO emission suffers from cloud absorption along the minor axis of the disk but there is weak millimeter dust and $C^{17}O$ emission present here (also seen by Bruderer et al. (2014) in the $C^{17}O$ $J = 6 - 5$). Previous studies have shown asymmetric emission for SO, SO_2, NO, and several of the large organics (Booth et al. 2021a; van der Marel et al. 2021a; Brunken et al. 2022). Here, we present the first detections of the simple molecules HCO^+, HCN, and CS and interestingly find that they all show a similar asymmetric emission morphology. However, not all of the molecules have the exact same asymmetric morphology.

3.3. Substructures in the IRS 48 Disk

The only molecule detected in the north of the IRS 48 disk is CO, while all of the other species are located in the south, but there are variations in where the different molecules peak both radially and azimuthally. Figure 3 shows azimuthal profiles taken from the intensity maps in Figure 2 at the radius where each of the molecules peaks along with the normalized azimuthal profile of the millimeter dust. From this, it is clear that there are dips in the intensity of most species at the

Table 2
Molecules Detected (✓) and not Detected (-) in the ALMA Observations of the IRS 48 and HD 100546 Disks Presented in this Paper and Booth et al. (2024)

Molecule	HD 100546	IRS 48
^{12}CO	✓	✓
$C^{17}O$	✓	✓
HCO^+	✓	✓
$HC^{18}O^+$	-	-
CN	✓	-
HCN	✓	✓
$H^{13}CN$	✓	?
$HC^{15}N$	✓	-
NO	✓	✓
HC_3N	-	-
CH_3CN	-	-
C_2H	✓	-
c − C_3H2	-	-
CS	✓	✓
$C^{34}S$	✓	-
SO	✓	✓
^{34}SO	✓	✓
^{33}SO	-	✓
SO_2	✓	✓
OCS	-	-
H_2CS	✓	-
H_2CO	✓	✓
$H_2^{13}CO$	✓	✓
CH_3OH	✓	✓
CH_3OCHO	✓	✓
CH_3OCH_3	-	✓
c-H_2COCH_2	-	✓

Note. The presence of $H^{13}CN$ in IRS 48 is unclear (indicated with "?") due to line blending with SO_2.

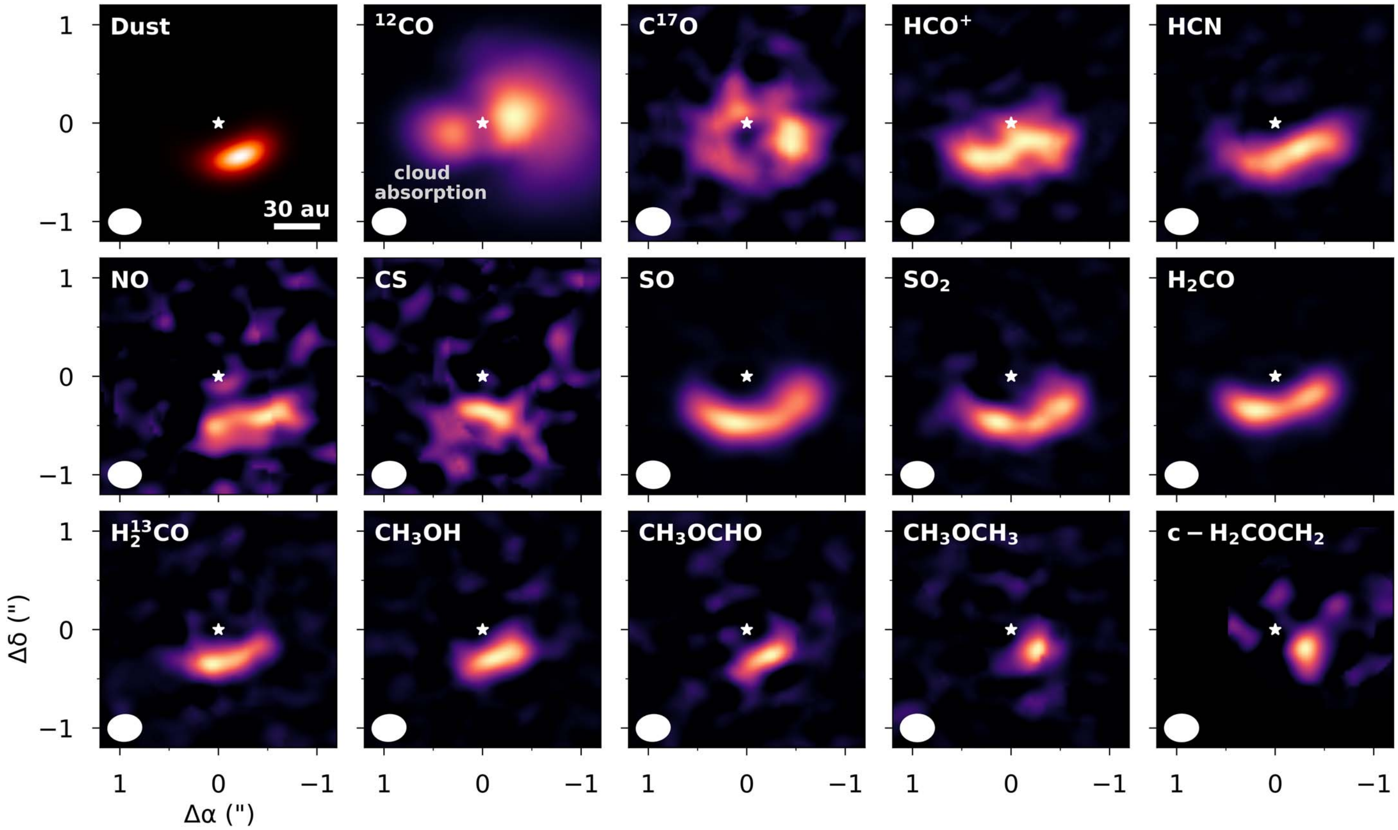

Figure 2. Integrated intensity maps of the 0.9 mm dust continuum emission and molecular line emission from the IRS 48 disk. The continuum map is shown on a color log scale to highlight the weak millimeter emission in the north of the disk. The beam is shown in the left-hand corner of each panel.

azimuthal peak of the dust emission. This could be due to line suppression from the optically thick dust (e.g., Weaver et al. 2018; De Simone et al. 2020), but interestingly this is not as apparent for the COM emission. The COM emission is also significantly narrower in the azimuthal extent than simpler molecules that are detected and are located at the dust peak with a similar width to the millimeter dust. This is highlighted further in Figure 4, which presents a polar deprojection of the intensity maps. It is clear that SO and SO_2 peak radially further out in the disk than CH_3OH and H_2CO, which was not clear in the lower spatial resolution data presented in van der Marel et al. (2021a) and Booth et al. (2021a). Furthermore, the HCO^+ emission is peaking closer to the star, in the gas cavity, than CH_3OH, and HCN is approximately co-spatial with H_2CO. The possible physical and chemical explanations for these different emission morphologies will be discussed further in Section 4.1.

3.4. Disk-integrated Line Fluxes

In Figure 5 we show the disk-integrated fluxes for molecules detected/nondetected in the IRS 48 disk compared to the HD 100546 disk, which was observed as part of the same ALMA program (Booth et al. 2024). For some molecules, we detected multiple transitions but we only report the flux of a representative transition. These representative transitions are based on the strongest lines detected in the HD 100546 disk. In the case of CN, C_2H, and NO, the chosen lines are the strongest of the $N = 3 - 2$, $N = 4 - 3$, and $J = 7/2 - 5/2$ hyperfine groups, respectively. For SO_2, $J = 6_{(4,2)} - 6_{(3,3)}$ is the strongest line detected, and for SO the $J = 7_8 - 6_7$ transition is the strongest. For CH_3OH we pick the $J = 7_0 - 6_0$ transition, and for CH_3OCHO and CH_3OCH_3 we use the $J = 3_1 - 3_0$ and $J = 19 - 18$ transitions which are both blends of multiple transitions. These fluxes are extracted from Keplerian masks that are 2.″0 and 4.″0 in radius for the IRS 48 and HD 100546 disks, respectively. If a molecule is undetected, we give the 3σ upper limit on the flux, where σ is propagated from the rms in the channel maps and the number of pixels included in the mask (e.g., Carney et al. 2019). All of the line fluxes are listed in Table 6 with their associated errors. After accounting for the different distances to the two sources (110 pc v 135 pc) HD 100546 is brighter in all of the lines aside from SO, ^{34}SO, SO_2, NO, $H_2^{13}CO$, CH_3OH, and CH_3OCHO. Note that the IRS 48 ^{12}CO ($J = 3 - 2$) flux is a lower limit due to foreground cloud absorption (e.g., see Figure 2 in Bruderer et al. 2014).

To account for the significantly different gas masses of the HD 100546 and IRS 48 disks (with HD 100546 >100× more massive than IRS 48; see Table 1), we normalize the line fluxes with respect to the C^{17}O $J = 3 - 2$ line. The C^{17}O line is the most optically thin CO isotopologue detected in both disks, and this flux should be a good proxy for the total gas content in each disk (e.g., Zhang et al. 2021). These flux ratios are shown in Figure 5, and from this, there are significant differences in the relative intensities of the different molecular lines between these two disks. There are caveats to this comparison, e.g., if lines are optically thick in one or both of the disks and/or the excitation temperatures are very different. This is, however, a good starting point for comparing the two sources. The observed line strengths of most of the simple molecules are within a factor of 3 for the two disks. The differences in the line ratios become more significant when looking at the molecules that are already brighter in IRS 48. There is a factor 15 difference for NO and

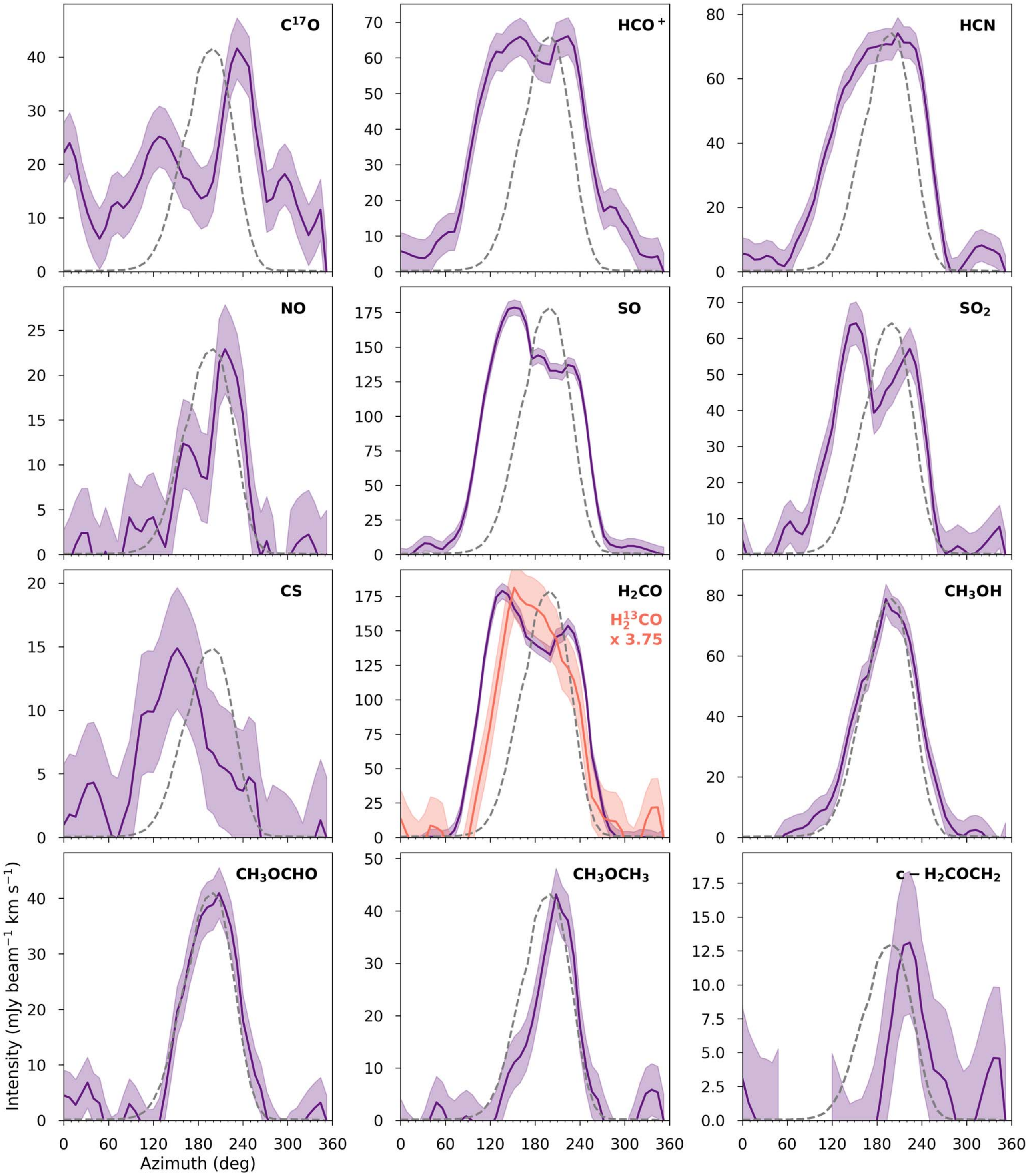

Figure 3. Azimuthal line emission profiles for the IRS 48 disk generated from the maps presented in Figure 2. The dashed lines show the millimeter dust emission normalized to the peak of the line emission in each panel.

CH_3OCHO, a factor 50 difference for SO, SO_2, and $H_2^{13}CO$, and a factor 80 difference for CH_3OH between the two disks. The largest difference is in the $^{34}SO/C^{17}O$ line ratio, which is $\approx 130\times$ higher in IRS 48 than HD 100546.

3.5. Column Densities

We estimate column densities following the methods outlined in Loomis et al. (2018a) and in the same manner as Booth et al. (2024). For the molecules where multiple transitions are detected, e.g., CH_3OH and SO_2, we pick one representative transition. Future work will focus specifically on constraining the excitation conditions of these molecules individually. We compute azimuthal column density profiles for the IRS 48 disk from the profiles presented in Figure 3 and explore a range of excitation temperatures: 50, 100, and 150 K. These temperatures are motivated by the observations and modeling results from van der Marel et al. (2021a) and Leemker et al. (2023). For the nondetected molecules, we

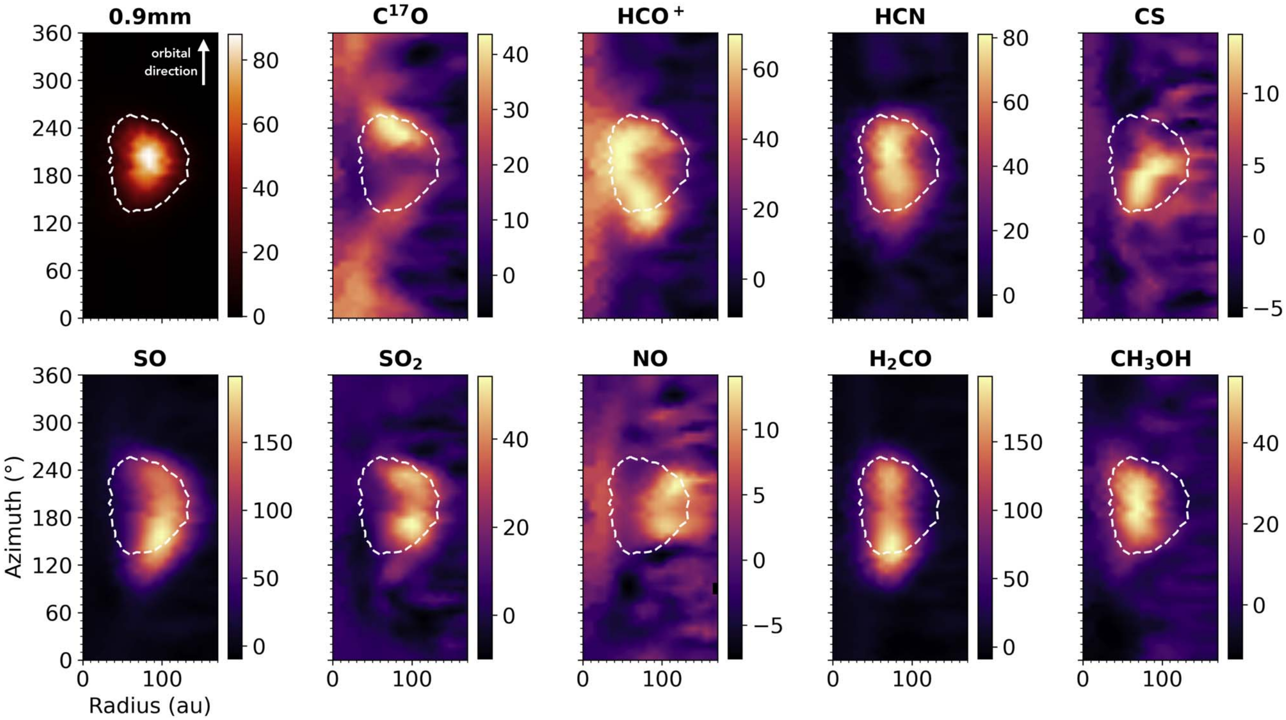

Figure 4. Polar deprojection of the IRS 48 integrated intensity maps that highlight the different emission morphologies compared to the dust. The dashed contour traces the 500σ level of the dust continuum emission. The units of the color bar are mJy beam^{-1} km s^{-1} for the molecular lines and mJy beam^{-1} for the continuum. The arrow highlights the direction of the disk rotation.

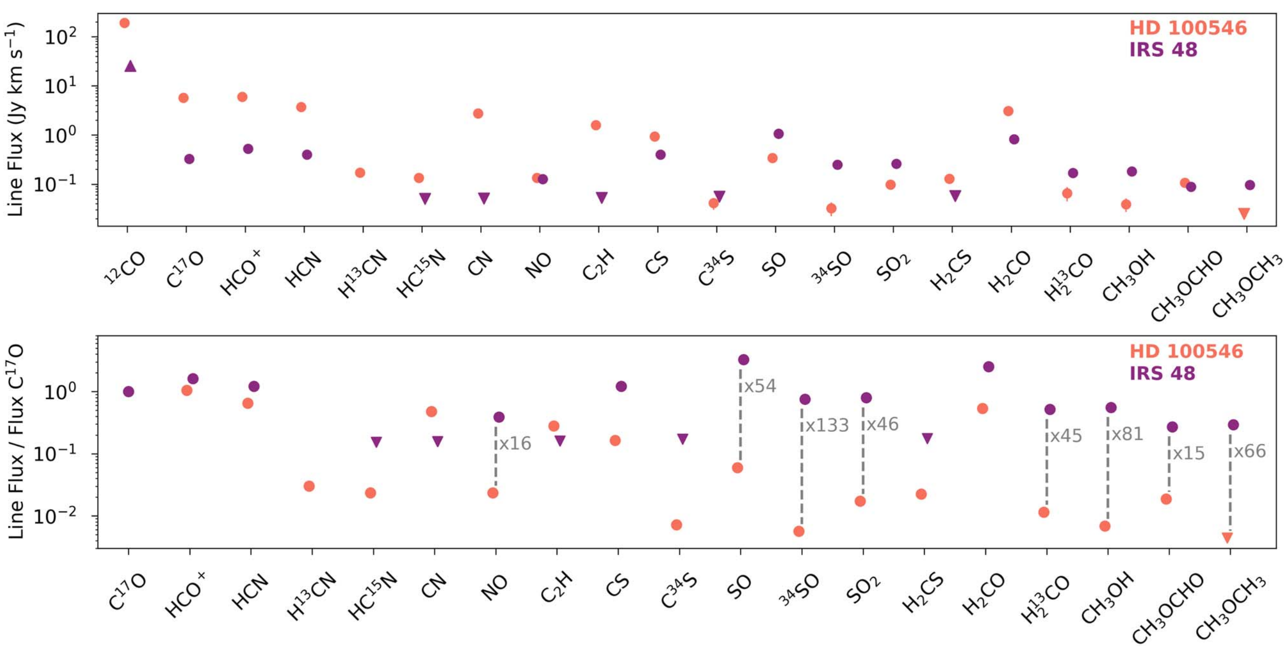

Figure 5. Top: disk-integrated fluxes for the molecules detected in the IRS 48 (purple) and HD 100546 (orange) disks. Bottom: disk-integrated fluxes relative to the $C^{17}O$ $J = 3 - 2$ line flux for each disk. Vertical lines and numbers show the relative differences in the different line ratios between each disk where this value is $>10\times$. Triangles pointing down are 3σ upper limits, and triangles pointing up are lower limits. For most of the lines, the $\pm 1\sigma$ error bars are smaller than the plot markers.

calculate an upper limit propagated from the upper limits on the disk-integrated fluxes (listed in Table 6) assuming a conservative emitting area of a 2″ aperture. The resulting profiles are shown in Figure 6, and the main results are as follows:

1. The peak $C^{17}O$ column density is $\approx 2.5 \times 10^{16}$ cm^{-2} at 100 K, and the line is optically thin. With the assumption of interstellar medium (ISM) isotope ratios, this is equivalent to a CO column density of $\approx 5 \times 10^{19}$ cm^{-2}. In Table 3 we list the peak column density ratios of each of the molecules relative to the average CO column density across the IRS 48 disk.
2. The line emission from the simple molecules HCO^+, HCN, and NO are all optically thin. CN and C_2H are both

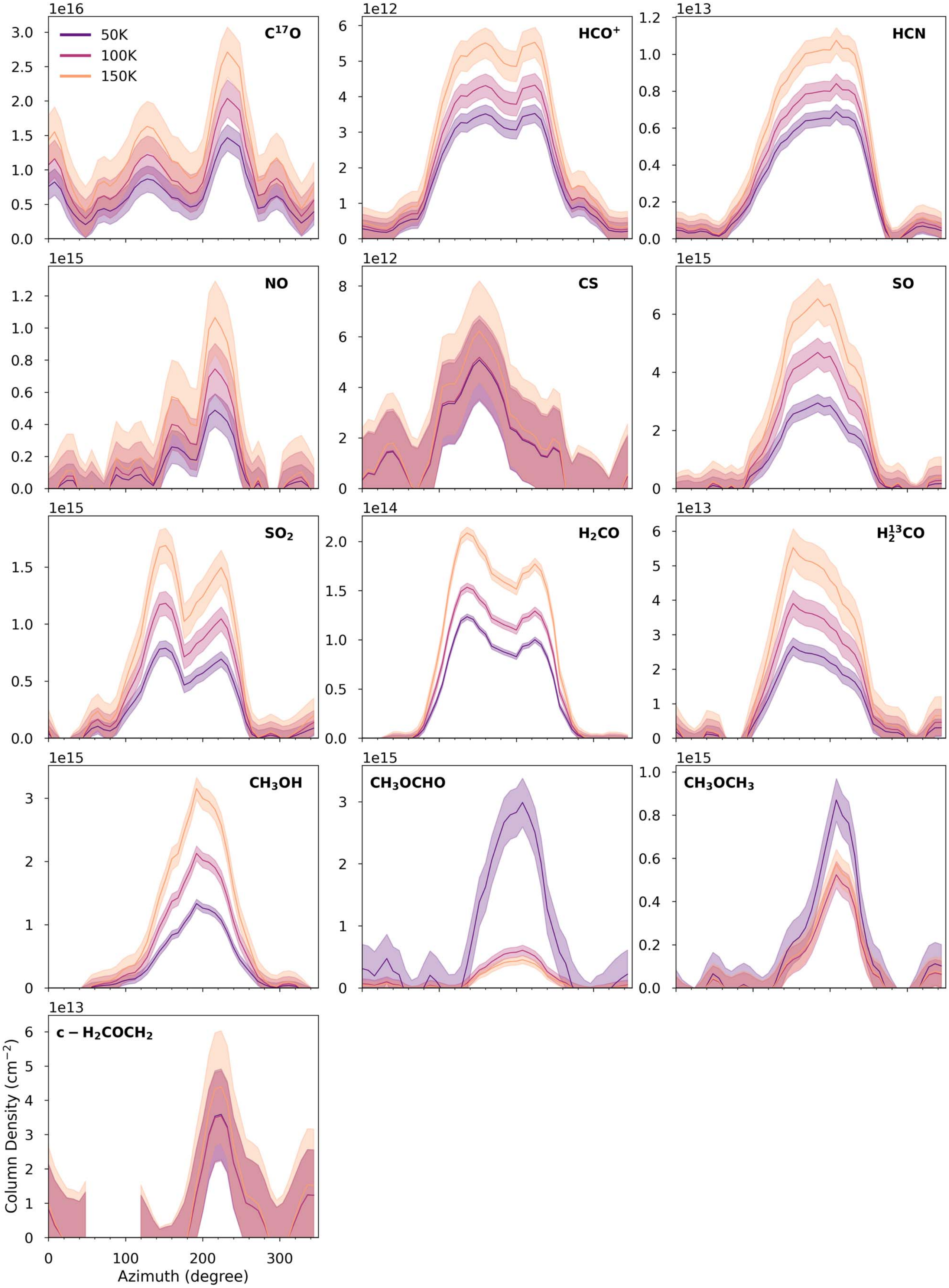

Figure 6. Azimuthal column density profiles for the IRS 48 disk determined at a range of assumed excitation temperatures.

Table 3
Ratios of the Peak Column Density of Different Molecules (X) Relative to Disk-averaged CO in the IRS 48 Disk

Molecule	N(X)/N(CO) $T_{ex} = 50$ K	N(X)/N(CO) $T_{ex} = 100$ K	N(X)/N(CO) $T_{ex} = 150$ K
HCO^+	$2.8 \pm 0.9 \times 10^{-7}$	$2.4 \pm 0.8 \times 10^{-7}$	$2.3 \pm 0.8 \times 10^{-7}$
HCN	$5.0 \pm 2.0 \times 10^{-7}$	$5.0 \pm 2.0 \times 10^{-7}$	$5.0 \pm 2.0 \times 10^{-7}$
CN	$<2.0 \times 10^{-8}$	$<2.0 \times 10^{-8}$	$<2.0 \times 10^{-8}$
NO	$4.0 \pm 1.0 \times 10^{-5}$	$4.0 \pm 2.0 \times 10^{-5}$	$4.0 \pm 2.0 \times 10^{-5}$
C_2H	$<5.0 \times 10^{-7}$	$<5.0 \times 10^{-7}$	$<5.0 \times 10^{-7}$
CS	$4.0 \pm 2.0 \times 10^{-7}$	$3.0 \pm 1.0 \times 10^{-7}$	$3.0 \pm 1.0 \times 10^{-7}$
SO	$2.3 \pm 0.7 \times 10^{-4}$	$2.6 \pm 0.8 \times 10^{-4}$	$2.7 \pm 0.9 \times 10^{-4}$
SO_2	$6.0 \pm 2.0 \times 10^{-5}$	$6.0 \pm 2.0 \times 10^{-5}$	$2.0 \pm 0.6 \times 10^{-5}$
H_2CO	$1.0 \pm 0.3 \times 10^{-5}$	$9.0 \pm 3.0 \times 10^{-6}$	$9.0 \pm 3.0 \times 10^{-6}$
$H_2^{13}CO$	$2.1 \pm 0.7 \times 10^{-6}$	$2.1 \pm 0.7 \times 10^{-6}$	$9.0 \pm 3.0 \times 10^{-7}$
CH_3OH	$1.1 \pm 0.3 \times 10^{-5}$	$1.2 \pm 0.4 \times 10^{-5}$	$1.3 \pm 0.4 \times 10^{-5}$
CH_3OCHO	$2.4 \pm 0.8 \times 10^{-4}$	$3.0 \pm 1.0 \times 10^{-5}$	$1.9 \pm 0.6 \times 10^{-5}$
CH_3OCH_3	$7.0 \pm 2.0 \times 10^{-5}$	$2.9 \pm 0.9 \times 10^{-5}$	$2.4 \pm 0.8 \times 10^{-5}$
c-H_2COCH_2	$3.0 \pm 1.0 \times 10^{-6}$	$2.0 \pm 1.0 \times 10^{-6}$	$2.0 \pm 1.0 \times 10^{-6}$
CO average	$1.3 \pm 0.4 \times 10^{19}$	$1.8 \pm 0.4 \times 10^{19}$	$2.3 \pm 0.8 \times 10^{19}$

Note. These peak values are all taken at different radial and azimuthal locations and are all relative to the average CO column density derived from the $C^{17}O$, not the peak $C^{17}O$ column density.

undetected with the 3σ disk-averaged upper limit of CN $\leqslant 2 \times 10^{12}$ cm^{-2} and $C_2H \leqslant 5 \times 10^{13}$ cm^{-2}.

3. The radical CS is detected with a peak column density of $\approx 10^{13}$ cm^{-2}, which is a factor of a few lower than the upper limit reported by Booth et al. (2021a). H_2CS is not detected with a column density upper limit of $<2 \times 10^{13}$ cm^{-2}, which relative to CS is not constraining when compared to other disks.
4. SO is abundant in the IRS 48 disk, and therefore we use the $J = 3_3 - 3_2$ transition for the column density calculation. This line has the lowest Einstein coefficient of the three SO transitions detected. The other two SO lines have lower column densities due to their higher optical depths. This results in a peak column density of 5×10^{15} cm^{-2} at 100 K. This is $\approx 4 \times$ higher than the SO_2 peak column density and results in N(CS)/N(SO)$\approx 10^{-3}$. When comparing the derived SO column density with the ^{34}SO column density, the ratio is consistent with 22, the local ISM ^{32}S–^{34}S ratio (Wilson 1999), indicating the $J = 3_3 - 3_2$ line is indeed optically thin. A detailed analysis of the S isotopes detected in these data will follow in future work. OCS is not detected with a column density upper limit of $<10^{12}$ cm^{-2}, less than a few percent of the SO column density.
5. Both H_2CO and $H_2^{13}CO$ are robustly detected, and we find a $H_2CO/H_2^{13}CO$ column density ratio of ≈ 4. This is significantly lower than the expected $^{12}C/^{13}C$ of 69 (Wilson 1999), indicating optically thick H_2CO emission or a lower isotope ratio.
6. The CH_3OH column density peaks at $\approx 2 \times 10^{15}$cm^{-2}. Using the column density derived for the main H_2CO isotopologue results in a column density ratio of CH_3OH/H_2CO of 14 ± 1 and using the $H_2^{13}CO$ and a C isotope ratio of 69 results in a ratio of 0.8 ± 0.1. This means that if the H_2CO is indeed optically thick the ratio of CH_3OH to H_2CO is ≈ 1. The CH_3OH emission is still compact in these new data; therefore, as discussed in Brunken et al. (2022), the emission may be optically thick and beam diluted. This will be investigated further in M. Temmink et al. (2024, in preparation) along with the constraints from 13CH_3OH, which remains undetected.
7. The peak abundance ratios of the COMs CH_3OCHO, CH_3OCH_3, and c-H_2COCH_2 with respect to the peak CH_3OH column density are 0.28 ± 0.04, 0.25 ± 0.03, and 0.017 ± 0.006, respectively, at a temperature of 100 K. CH_3CHO is undetected with an upper limit of $\approx 4 \times 10^{13}$ cm^{-2}.

4. Discussion

In this section, we discuss the physical and chemical origins of the observed molecular emission in the IRS 48 disk. We place this unique source in context with another chemically well-characterized protoplanetary disk, namely, the HD 100546 disk, which has been observed in the same frequency setting within the same ALMA program.

4.1. The Origin of the Molecular Substructures in the IRS 48 Disk

The simplest explanation for the molecular complexity and high relative column densities of oxygen-bearing volatiles in the IRS 48 disk is the sublimation of ices. With these new data, there are clear spatial offsets between the different molecules that complicate this picture. As seen in Figures 2 and 4, the COMs have the most compact emission that peaks with the dust, and these are also the species with the highest binding energies. The H_2CO and HCN emissions are roughly co-spatial with a depression in both the H_2CO and HCO^+ emissions where the COM (and dust) emission is the brightest. Interestingly, the SO and SO_2 emissions, which Booth et al. (2021a) proposed originate from the sublimation and photodissociation of H_2O and H_2S to OH and S, respectively, are peaking radially further out in the disk compared to the CH_3OH, the latter of which should trace the same region as the H_2O. This may point to a different chemical origin for SO and SO_2. There may also be a link between gas leading and trailing in the Keplerian orbit of the dust trap. The orbital direction is highlighted in Figure 4. The dust trap in the IRS 48 disk has been proposed to be a large anticyclonic vortex (van der Marel et al. 2013); therefore, it could be expected that there is additional radial and vertical mixing, or turbulence, and this will affect the disk chemistry. Semenov & Wiebe (2011) find that in their turbulent disk chemistry models the abundances of SO and SO_2 can increase by 2 orders of magnitude relative to the laminar disk due to the enhanced sublimation of ices. The interplay between the dust and line optical depth may also be influencing the observed emission structures. Therefore, a more detailed analysis of the IRS 48 line emission, including mapping the disk temperature structure, will be the focus of future work (M. Temmink et al. 2024, in preparation).

4.2. In Context with other Herbig Disks

Both the IRS 48 and HD 100546 disks show rich reservoirs of complex organics and volatile sulfur that are yet to be detected in most other planet-forming disks (aside from HD 169142; Booth et al. 2023). The simplest explanation for the chemical origin of these species is via the sublimation of H_2O and COM-rich ices. The brightness temperatures of the

^{12}CO in these disks are 100 K indicating the physical conditions for ice sublimation are indeed possible (see Wölfer et al. 2023). There are significant differences between the two disks, especially when considering their masses and sizes. The HD 100546 disk has a gas mass 500× and dust mass 100× higher than those of the IRS 48 disk (see Table 1), and the HD 100546 CO disk extends to ≈600 au compared to ≈200 au for IRS 48. Given the different mass reservoirs in the disks, one may expect IRS 48 to have uniformly lower line fluxes than HD 100546 but, as shown in Figure 5, this is not the case. On a disk average level the relative fluxes of simple oxygen molecules (NO, SO, SO_2) and larger organics (H_2CO, COMs) are 15–130 times brighter in IRS 48 than HD 100546.

The HCO^+ abundance in the IRS 48 disk is similarly low as found in HD 100546 and HD 142527, which is 2 orders of magnitude lower than found in the HD 163296 and MWC 480 disks (see Table 4; Aikawa et al. 2021; Temmink et al. 2023; Booth et al. 2024, priv. comm. Temmink). This may be due to the low stellar X-ray flux of IRS 48 and/or the presence of gas-phase H_2O (not yet detected in IRS 48 but only inferred; Leemker et al. 2023), which effectively destroys HCO^+. We do not detect CN in IRS 48, and similar to HD 100546 it has a low CN/HCN ratio when compared to other disks. The low CS/SO ratio and nondetection of C_2H are consistent with a disk C/O<1, as reported by Booth et al. (2021a). Similar to HD 100546, NO is the most abundant observed nitrogen carrier in the IRS 48 disk when compared to HCN or CN. The sulfur-bearing equivalent of H_2CO, H_2CS, was not detected in IRS 48. Given the high abundance of H_2CO in IRS 48 this may be surprising, but in the HD 100546 disk, the H_2CS follows the CS (as also found in MWC 480 and HD 169142; Le Gal et al. 2021; Booth et al. 2023) and not the sublimating SO in the inner disk. This indicates that the H_2CS in disks is likely forming in the gas phase at lower temperatures (<100 K) rather than having a significant abundance on the grains.

4.3. Contextualizing the Volatile Sulfur Reservoir in the IRS 48 Disk

In IRS 48, SO, SO_2, and CS are detected, but OCS and H_2CS are not. With this family of molecules, we can compare the relative column density ratios of these species to both protostars and comets. In IRS 48, SO is the most abundant S-bearing volatile detected with peak column density ratios of SO_2/SO of ≈26%, CS/SO of ≈0.2%, OCS/SO of <0.3%, and H_2CS/SO of <1.0%. The SO_2/SO ratio in IRS 48 is similar to that detected in HD 100546 where again the SO column density is higher than the SO_2 column density (Booth et al. 2024), but this is not the same as observed toward both protostars and comets. Drozdovskaya et al. (2018) compare the volatile sulfur reservoirs in comet 67P and toward the protostar IRAS 16293-2422 B. Comparing these environments to IRS 48: SO_2, OCS, and H_2CS are all lower in abundance relative to SO in this disk than could be expected from the sublimation of cometary ices, although the SO/SO_2 ratio from 67 P has been shown to vary in time, exceeding 1 at points (Calmonte et al. 2016). Additionally, Drozdovskaya et al. (2018) show that OCS has strong variations between these two environments with OCS/SO ≈60% in 67P and ≈560% in IRAS 16293-2422 B, where in the latter source OCS is proposed to be enhanced due to UV irradiation. For both ratios, OCS would have been detectable in our data of the IRS 48 (and HD 100546) disk. Boogert et al. (2022) find that the column density of OCS in the ices toward massive young stellar objects (MYSOs) correlates with the abundance of CH_3OH ice. Therefore, with the detection of CH_3OH in IRS 48 we may expect to also see OCS if these ices are dually inherited by the disk, but the binding energy of OCS (pure ice, 2430 K; Ward et al. 2012) is significantly lower than that of CH_3OH (water ice, 5000 K; Ferrero et al. 2020; Minissale et al. 2022). The median ice abundance of OCS relative to CH_3OH toward the MYSO target by Boogert et al. (2022) is ≈1%, and in contrast for IRS 48, we find that the gas-phase column density ratio of OCS/CH_3OH is <0.1%. One explanation for the lack of OCS could be that during the disk lifetime, the volatile S in the simple inherited ices is converted to more refractory compounds like S allotropes due to processing via UV irradiation (Cazaux et al. 2022). Formation of S allotropes can also act to destroy OCS on the ice, with models showing that OCS + S $\rightarrow S_2$ + CO can be an important destruction pathway for OCS ice (Laas & Caselli 2019). If S_2 is desorbed from grains, it can also play an important role in gas-phase SO (and SO2) formation, via reactions with atomic O. All in all, these comparisons show that the gas-phase volatile sulfur in IRS 48 is distinct to both the gas and ice detected toward protostars and in comets.

4.4. Molecular Complexity as Evidence for Ice Processing?

The degree of molecular complexity detected in the IRS 48 disk is unique for protoplanetary disks with three ⩾7 atom COMs detected—CH_3OCHO, CH_3OCH_3, and c-H_2COCH_2. c-H_2COCH_2 is the first detection of a heterocyclic molecule in a protoplanetary disk. Heterocycles are abundant in comet 67P (Hänni et al. 2023), and more generally these rings of carbon with oxygen are of biological importance. The peak abundance ratios of these COMs with respect to the peak CH_3OH column density show that these COMs have abundances of ≈30%, 25%, and 2% of CH_3OH, respectively. Similarly, in the HD 100546 disk, in addition to CH_3OH, CH_3OCHO is also detected with an abundance of 70% relative to CH_3OH. Interestingly, CH_3OCH_3 is undetected in HD 100546 with an upper limit of ≲10% relative to CH_3OH. The slight differences in the binding energies of CH_3OCHO and CH_3OCH_3 are not sufficient to explain the lack of CH_3OCH_3 in HD 100546 as they are both lower than the binding energy of CH_3OH (Minissale et al. 2022; Ligterink & Minissale 2023).

Typically, in the warm gas around low- and high-mass protostars, these COMs have fractional abundances of a few percent of CH_3OH (e.g., Manigand et al. 2020; van Gelder et al. 2020; Chen et al. 2023). The higher abundances we see in Class II disks may simply be due to an underestimated CH_3OH column density due to optically thick and beam-diluted line emission. Deeper observations to target $^{13}CH_3OH$ isotopologues are needed to test this. Otherwise, if these high ratios are confirmed, these results reflect a different chemistry than is traced in observations of protostars. Similarly, the abundance ratio of CH_3OCHO to CH_3OCH_3 has been shown to be remarkably constant across different evolutionary stages of star formation (Coletta et al. 2020; Chen et al. 2023). This ratio of ≈1 is also seen in IRS 48 but not for HD 100546 where we find a ratio of ≳7. c-H_2COCH_2 is an isomer of acetaldehyde (CH_3CHO) and vinyl alcohol (CH_2CHOH), both of which are undetected in our data. CH_3CHO is typically the most abundant of these isomers by at least an order of magnitude: for example, observations of IRAS 16293-2422 find that CH_3CHO is ≈10× more abundant than c-H_2COCH_2 and c-H_2COCH_2 relative to

CH_3OH is ≈0.05% (Lykke et al. 2017; Manigand et al. 2020), whereas, in IRS 48, $CH_3CHO/c\text{-}H_2COCH_2 \lesssim 1$.

The high abundance ratios of COMs with respect to CH_3OH that we have observed so far in Class II disks and the variation in CH_3OCHO and CH_3OCH_3 ratios between sources could be the result of the energetic processing of ices in disks. Over the millions of years that ices have been present in disks, they will be exposed to UV photons, X-rays, and cosmic rays—especially if vertical mixing is prominent. These energetic processes can break apart CH_3OH ice resulting in radicals (CH_3O, HCO, CH_3) that can combine to form the more complex species CH_3OCHO, CH_3OCH_3, and CH_3CHO (Öberg et al. 2009). The specific branching ratios for these radicals will play a key role in setting the new COM ice abundances (Laas et al. 2011; Walsh et al. 2014a). c-H_2COCH_2 has been shown to form in the solid state via the reaction of C_2H_4 and O, where Bergner et al. (2019) find a branching ratio of 0.5 for c-H_2COCH_2 relative to CH_3CHO. Given the upper limit on CH_3CHO in the IRS 48 disk, this may indicate that the formation of COMs via oxygen insertion reactions is also important. Finally, there may also be a nonnegligible contribution from gas-phase reactions in the inner disk where the gas is warm >100 K, UV irradiated, and at a significantly higher density than in protostellar envelopes. This needs to be tested with astrochemical models, which we leave to further work. Additionally, a larger sample of disks is needed to understand the spread of COM abundances in disks and better place IRS 48 in context. Upper limits on other COMs lines covered in these data and deuterated isotopes, e.g., HDCO, in the IRS 48 disk, will be investigated in Kipfer et al. (2024, in preparation), where a further, more complete comparison to protostellar environments and comets will be made.

5. Conclusion

This paper is the second in a series presenting an ALMA molecular line survey of the disks around the Herbig Ae stars HD 100546 and IRS 48. Here we focus on the IRS 48 disk where we detect 16 different molecular species, and our main results are as follows:

1. We report the first robust detections of $H_2^{13}CO$, ^{34}SO, ^{33}SO, and c-H_2COCH_3 in protoplanetary disks and confirm that the reported tentative detection of CH_3OCHO from Brunken et al. (2022) and CH_3OCH_3 is clearly seen. We also detect the simple molecules HCO^+, HCN, and CS in the IRS 48 disk for the first time.
2. The IRS 48 disk hosts an extremely asymmetric dust trap in the south of the disk. We find that all the molecular lines detected aside from CO show emission in the same region of the disk as the dust trap, including the simple molecules HCO^+, HCN, and CS.
3. The asymmetric molecular emissions from the different molecules are not all co-spatial. There are radial and azimuthal offsets in the peak position most clearly seen between the COMs and the SO and SO_2. This warrants further investigation of the chemistry in turbulent vortices.
4. The low relative abundance of HCO^+ in IRS 48 is similar to the other Herbig disks HD 100546 and HD 142527, which could reflect the star's lower X-ray luminosity when compared to other sources. Similar to regions of the HD 100546 disk, the CN/HCN ratio in IRS 48 is low <1, where the lack of CN may also be due to the low C/O ratio in the IRS 48 disk gas (Leemker et al. 2023). This is distinct from the elemental makeup in the other Herbig Ae disks, HD 163296 and MWC 480.
5. CS and HCN are the only molecules detected in the IRS 48 disk without oxygen, and the low CS/SO ratio and the nondetection of C_2H support the bulk of the gas south of the IRS 48 disk having C/O<1. In these data, there is no evidence of an enhanced C/O>1 in the nondust trap region of the disk. Furthermore, the partition of volatile S between SO, SO_2, and CS and the nondetected OCS and H_2CS is distinct from that measured for comets and protostars with OCS/SO <0.3%.
6. IRS 48 hosts the most chemically complex disk to date and the high abundances of COMs relative to CH_3OH when compared to protostars as well as the different relative COMs ratios may indicate processing of the inherited ices in protoplanetary disks. The apparently high column density ratios of COMs to CH_3OH need to be confirmed via observations of optically thin tracers of CH_3OH, i.e., the ^{13}C isotopologues.

Our results solidify the IRS 48 disk as a unique astrochemical laboratory to study the full volatile reservoir available during planet formation and show the benefits of large unbiased surveys of protoplanetary disks. The clear association of the molecular emissions with the dust trap shows a strong coupling between the dust and ice chemistry. Nine different molecules have been detected for the first time in the IRS 48 disk in only two ALMA observing programs (2017.1.00834.S, 2021.1.00738) with just ≈10 hr of on-source time. The efficiency of these types of observations will improve dramatically with the planned Wideband Sensitivity Upgrade for ALMA, which will increase both the simultaneously observable bandwidth and the imaging speed (Carpenter et al. 2023).

Acknowledgments

This paper makes use of the following ALMA data: 2021.1.00738.S. We acknowledge assistance from Allegro, the European ALMA Regional Centre node in the Netherlands. ALMA is a partnership of ESO (representing its member states), NSF (USA), and NINS (Japan), together with NRC (Canada), MOST and ASIAA (Taiwan), and KASI (Republic of Korea), in cooperation with the Republic of Chile. The Joint ALMA Observatory is operated by ESO, AUI/NRAO, and NAOJ. This work has used the following additional software packages that have not been referred to in the main text: Astropy, IPython, Jupyter, Matplotlib, and NumPy (Hunter 2007; Pérez & Granger 2007; Kluyver et al. 2016; Harris et al. 2020; Astropy Collaboration et al. 2022). Astrochemistry in Leiden is supported by funding from the European Research Council (ERC) under the European Union's Horizon 2020 research and innovation program (grant agreement No. 101019751 MOLDISK). A.S.B. is supported by a Clay Postdoctoral Fellowship from the Smithsonian Astrophysical Observatory. M.L. acknowledges support from grant 618.000.001 from the Dutch Research Council (NWO). J.I.D. acknowledges support from an STFC Ernest Rutherford Fellowship (ST/W004119/1) and a University Academic Fellowship from the University of Leeds. M.T. acknowledges support from the ERC grant 101019751 MOLDISK. C.W. acknowledges financial support from the University of Leeds, the Science and Technology Facilities Council, and UK Research and Innovation (grant Nos. ST/X001016/1 and MR/T040726/1). L.E. acknowledges financial support from the Science and Technology Facilities Council (grant No. ST/T000287/1). S.N. is grateful for support from the RIKEN Special Postdoctoral Researcher Program (Fellowships), Grants-in-Aid for JSPS (Japan Society for the Promotion of Science) Fellows grant No. JP23KJ0329 and MEXT/JSPS Grants-in-Aid for Scientific Research (KAKENHI) grant Nos. JP 18H05441, JP20K22376, JP20H05845, JP20H05847, JP23K13155, and JP23H05441. Support for C.J.L. was provided by NASA through the NASA Hubble Fellowship grant No. HST-HF2-51535.001-A awarded by the Space Telescope Science Institute, which is operated by the Association of Universities for Research in Astronomy, Inc., for NASA, under contract NAS5-26555. The National Radio Astronomy Observatory is a facility of the National Science Foundation operated under cooperative agreement by Associated Universities, Inc.

Appendix A
Observational Setup of IRS 48

Table 4 lists the execution blocks of the ALMA data of the IRS 48 disk from program 2021.100738.S.

Table 4
Execution Block Details

Setting	Date	No. Antenna[a]	Integration Time (minutes)	Baselines (m)	Mean PVW (mm)	MRS (″)	Phase Calibrator	Flux/Bandpass Calibrator
A	30-05-2022	43	69	15.1–783.5	1.0	4.0	J1626-2951	J1517-2422
	08-06-2022	41	72	15.1–783.5	0.6	3.9	J1626-2951	J1427-4206
	08-06-2022	39	70	15.1–783.5	0.5	3.6	J1626-2951	J1427-4206
B	28-05-2022	45	73	15.1–783.5	1.2	3.6	J1626-2951	J1517-2422
	28-05-2022	44	57	15.1–783.5	0.9	3.6	J1626-2951	J1517-2422
	28-05-2022	43	73	15.1–783.5	0.9	4.0	J1626-2951	J1517-2422
	29-05-2022	44	73	15.1–783.5	1.4	3.9	J1626-2951	J1517-2422
	30-05-2022	43	73	15.1–783.5	0.9	4.1	J1626-2951	J1517-2422

Note.
[a] Number of antennae after flagging.

Appendix B
Molecular Data

The properties of the molecular transitions analysed in this work are listed in Table 5.

Table 5
Molecular Data of the Transitions Presented in this Paper

Molecule	Transition	Frequency (GHz)	E_{up} (K)	log10(A_{ul})	g_u	Detection
^{12}CO	$J = 3 - 2$	345.7959899	33.2	−5.6027	7	✓
$C^{17}O$	$J = 3 - 2$	337.0611298	32.7	−5.6344	7	✓
HCO^+	$J = 4 - 3$	356.7342230	42.8	−2.4471	9	✓
HCN	$J = 4 - 3$	354.5054779	42.5	−2.6860	27	✓
$H^{13}CN$	$J = 4 - 3$	345.3397693	41.4	−2.7216	27	-
$HC^{15}N$	$J = 4 - 3$	344.2001089	41.3	−2.7258	9	-
CN	$J = 7/2 - 5/2,\ F = 7/2 - 5/2$	340.2477700	32.7	−3.3839	10	-
	$J = 7/2 - 5/2,\ F = 7/2 - 5/2$	340.2477700	32.7	−3.4206	8	-
	$J = 7/2 - 5/2,\ F = 5/2 - 3/2$	340.2485440	32.7	−3.4347	6	-
NO	$J = 7/2 - 5/2,\ \Omega = 1/2 - F = 9/2 - 7/2$	351.0435240	36.1	−5.2649	10	✓
	$J = 7/2 - 5/2,\ \Omega = 1/2 - F = 7/2 - 5/2$	351.0517050	36.1	−5.2662	8	✓
	$J = 7/2 - 5/2,\ \Omega = 1/2 - F = 7/2 - 5/2$	351.0517050	36.1	−5.3161	6	✓
HC_3N	$J = 38 - 37$	345.6090100	323.5	−2.4812	77	-
	$J = 39 - 38$	354.6974631	340.5	−2.4473	79	-
CH_3CN	$J = 19_0 - 18_0$	349.4536999	167.7	−2.5909	78	-
C_2H	$J = 9/2 - 7/2,\ F = 5 - 4$	349.3374558	41.9	−3.7247	11	✓
	$J = 9/2 - 7/2,\ F = 4 - 3$	349.3387284	41.9	−3.7349	9	✓
CS	$J = 7 - 6$	342.8828503	65.8	−3.0774	15	✓
H_2CS	$J = 10_{(1,10)} - 9_{(1,9)}$	338.0831953	102.4	−3.1995	63	-
SO	$J = 3_3 - 3_2$	339.3414590	25.5	−4.8372	7	✓
	$J = 7_8 - 6_7$	340.7141550	81.2	−3.3023	15	✓
	$J = 8_8 - 7_7$	344.3106120	87.5	−3.2852	17	✓
^{34}SO	$J = 8_8 - 7_7$	337.5801467	77.3	−3.3109	17	✓
	$J = 9_8 - 8_7$	339.8572694	86.1	−3.2944	19	✓
^{33}SO	$J = 9_8 - 8_7\ F = 21/2 - 19/2$	343.0882949	78.0	−3.2819	22	✓
	$J = 9_8 - 8_7\ F = 19/2 - 17/2$	343.0880780	78.0	−3.2896	20	✓
	$J = 9_8 - 8_7\ F = 17/2 - 15/2$	343.0861019	78.0	−3.2934	18	✓
	$J = 9_8 - 8_7\ F = 15/2 - 13/2$	343.0872979	78.0	−3.2916	16	✓
	$J = 7_8 - 6_7\ F = 17/2 - 15/2$	337.1986199	80.5	−3.3158	18	✓
	$J = 7_8 - 6_7\ F = 15/2 - 13/2$	337.1978453	80.5	−3.3283	16	✓
	$J = 7_8 - 6_7\ F = 13/2 - 11/2$	337.1980219	80.5	−3.3351	14	✓
	$J = 7_8 - 6_7\ F = 11/2 - 9/2$	337.1993711	80.5	−3.3328	12	✓
SO_2	$J = 6_{(4,2)} - 6_{(3,3)}$	357.9258478	58.6	−3.5845	13	✓
OCS	$J = 28 - 27$	340.4492733	237.0	−3.9378	57	-
	$J = 29 - 28$	352.5995703	253.9	−3.8918	59	-
H_2CO	$J = 5_{(1,5)} - 4_{(1,4)}$	351.7686450	62.5	−2.9201	33	✓
$H_2^{13}CO$	$J = 5_{(1,5)} - 4_{(1,4)}$	343.3257130	61.3	−2.9517	33	✓
CH_3OH	$J = 7_0 - 6_0$	338.4086980	65.0	−3.7691	60	✓
CH_3OCHO	$J = 32_{(2,31)} - 31_{(2,30)}$	344.0297653	276.1	−3.2099	65	✓
	$J = 32_{(1,32)} - 31_{(1,31)}$	344.0297645	276.1	−3.2099	65	✓
	$J = 32_{(0,32)} - 31_{(0,31)}$	344.0295703	276.1	−3.2099	65	✓
	$J = 32_{(1,32)} - 31_{(1,31)}$	344.0295694	276.1	−3.2099	65	✓
CH_3OCH_3	$J = 19_{(0,19)} - 18_{(1,18)}$ AE	342.6080601	167.1	−3.2816	117	✓
	$J = 19_{(0,19)} - 18_{(1,18)}$ EA	342.6080602	167.1	−3.2817	78	✓
	$J = 19_{(0,19)} - 18_{(1,18)}$ EE	342.6081188	167.1	−3.2816	312	✓
	$J = 19_{(0,19)} - 18_{(1,18)}$ AA	342.6081774	167.1	−3.2816	195	✓
CH_3CHO	$J = 18_{(3,15)} - 17_{(3,14)}$ A	350.1334296	179.2	−2.82551	74	…
	$J = 18_{(3,15)} - 17_{(3,14)}$ E	350.1343816	179.2	−2.82596	74	…
c-H_2COCH_2	$J = 11_{(1,10)} - 10_{(2,9)}$ (ortho)	338.77197600	104.0	−3.19217	69	✓
	$J = 11_{(1,10)} - 10_{(2,9)}$ (para)	338.77197600	104.0	−3.19212	115	✓

Note. This covers all of the molecules detected in the disk and particular nondetections of interest but not all of the transitions covered/detected. All data are taken from CDMS except for $C^{17}O$, C_2H, CH_3OCHO, and CH_3OCH_3, which are from JPL (Pickett et al. 1998; Endres et al. 2016).

Appendix C
Image Properties

The properties of the tCLEAN line images presented in Figure 2 are listed in Table 6. This includes the beam size, channel map rms and peak flux, and the disk integrated flux.

Table 6
Properties of the Line Images for IRS 48 Presented in Figure 2 and Selected Nondetections

Molecule	Transition	Robust	Beam (″×″(°))	rms (mJy beam $^{-1}$)	Peak (mJy beam $^{-1}$)	Int. Flux (mJy beam km s^{-1})
^{12}CO	$J = 3 - 2$	0.5	0.34 × 0.26 (−85.3)	0.94	662.4	>25334.0
C^{17}O	$J = 3 - 2$	0.5	0.34 × 0.28 (−89.6)	1.2	19.2	328.0 ± 20.0
HCO^+	$J = 4 - 3$	0.5	0.33 × 0.26 (−84.1)	1.19	30.8	529.0 ± 21.0
HCN	$J = 4 - 3$	0.5	0.33 × 0.26 (−84.8)	1.04	29.5	400.0 ± 18.0
H^{13}CN	$J = 4 - 3$	0.5	0.34 × 0.26 (−85.2)	0.92	⋯	<48.0
HN^{15}N	$J = 4 - 3$	0.5	0.34 × 0.27 (−84.4)	0.99	⋯	<50.0
CN	$N = 4 - 3$	0.5	0.34 × 0.27 (87.9)	1.03	⋯	<52.0
HC_3N	$J = 38 - 37$	0.5	0.34 × 0.26 (−85.2)	0.94	⋯	<66.0
	$J = 39 - 38$	0.5	0.33 × 0.26 (−84.7)	1.04	⋯	<75.0
CH_3CN	$J = 19_0 = 18_0$	0.5	0.33 × 0.26 (−89.3)	1.05	⋯	<75.0
NO	$J = 7/2 - 5/2$	0.5	0.33 × 0.26 (−89.9)	1.08	8.16	127.0 ± 25.0
C_2H	$N = 4 - 3$	0.5	0.33 × 0.26 (−89.4)	1.02	⋯	<53.0
CS	$J = 7 - 6$	0.5	0.34 × 0.27 (−84.4)	1.03	5.82	40 ± 17.0
H_2CS	$J = 10_{(1,10)} - 9_{(1,9)}$	0.5	0.34 × 0.27 (−89.3)	1.16	⋯	<58.0
SO	$J = 3_3 - 3_2$	0.5	0.34 × 0.27 (87.9)	0.79	87.60	1070.0 ± 13.0
	$J = 7_8 - 6_7$	0.5	0.34 × 0.27 (−85.3)	1.0	84.96	1063.0 ± 23.0
	$J = 8_8 - 7_7$	0.5	0.34 × 0.27 (88.2)	1.05	27.85	232.0 ± 24.0
^{34}SO	$J = 8_8 - 7_7$	0.5	0.34 × 0.27 (88.0)	0.98	28.81	251.00 ± 22.0
	$J = 9_8 - 8_7$	0.5	0.34 × 0.27 (−89.4)	1.13	23.93	187.0 ± 26.0
^{33}SO	$J = 7_8 - 6_7$	0.5	0.34 × 0.27 (−84.5)	1.0	10.64	115.0 ± 23.0
	$J = 9_8 - 8_7$	0.5	0.34 × 0.28 (−89.5)	1.15	8.60	60.0 ± 20.0
SO_2	$J = 6_{(4,2)} - 6_{(3,3)}$	0.5	0.33 × 0.26 (−84.2)	0.88	26.83	261.0 ± 15.0
OCS	$J = 28 - 27$	0.5	0.34 × 0.27 (88.0)	0.98	⋯	<67.0
	$J = 27 - 26$	0.5	0.33 × 0.26 (-90.0)	1.42	⋯	<101
H_2CO	$J = 5_{(1,5)} - 4_{(1,4)}$	0.5	0.33 × 0.26 (90.0)	1.21	77.54	824.0 ± 21.0
$H_2^{13}CO$	$J = 5_{(1,5)} - 4_{(1,4)}$	0.5	0.34 × 0.27 (−84.5)	1.02	17.34	169.0 ± 17.0
CH_3OH	$J = 7_0 - 6_0$	0.5	0.34 × 0.27 (−89.5)	1.11	19.83	182.0 ± 18.0
CH_3OCHO	$J = 31 - 30$	0.5	0.34 × 0.27 (−84.4)	0.98	12.50	95.0 ± 23.0
CH_3OCH_3	$J = 19 - 28$	0.5	0.34 × 0.27 (−89.6)	0.82	13.14	87.0 ± 23.0
CH_3CHO	$J = 18_{(3,15)} - 17_{(3,14)}$	0.5	0.34 × 0.27 (−89.7)	0.79	⋯	<75
c-H_2COCH_2	$J = 11_{(1,10)} - 10_{(2,9)}$	2.0	0.37 × 0.3 (27.7)	0.77	5.70	39.0 ± 24

Appendix D
Full Spectrum Matched Filter Response

In Figure 7 we share a fully annotated version of the matched filter response for the IRS 48 disk with a 150 au Keplerian mask where we note all the detections of molecular lines at the 4σ level with this filter.

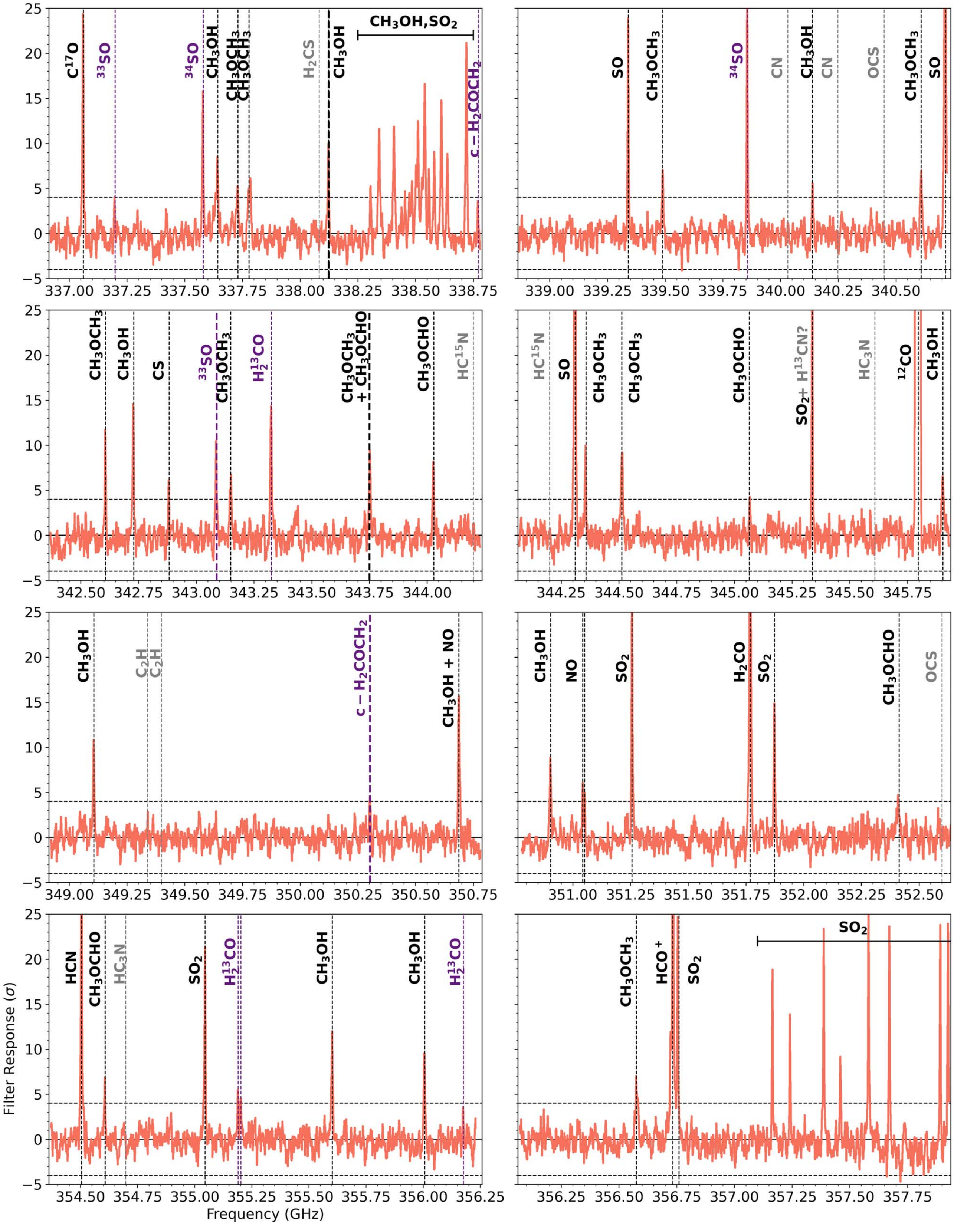

Figure 7. IRS 48 matched filter response using a 150 au in radius Keplerian model. Detected molecules/transitions above the 4σ level are labeled. New disk molecules are noted in purple, and notable nondetections are shown in gray.

ORCID iDs

Alice S. Booth https://orcid.org/0000-0003-2014-2121
Milou Temmink https://orcid.org/0000-0002-7935-7445
Ewine F. van Dishoeck https://orcid.org/0000-0001-7591-1907
Lucy Evans https://orcid.org/0009-0006-1929-3896
John D. Ilee https://orcid.org/0000-0003-1008-1142
Mihkel Kama https://orcid.org/0000-0003-0065-7267
Luke Keyte https://orcid.org/0000-0001-5849-577X
Charles J. Law https://orcid.org/0000-0003-1413-1776
Margot Leemker https://orcid.org/0000-0003-3674-7512
Nienke van der Marel https://orcid.org/0000-0003-2458-9756
Hideko Nomura https://orcid.org/0000-0002-7058-7682
Shota Notsu https://orcid.org/0000-0003-2493-912X
Karin Öberg https://orcid.org/0000-0001-8798-1347
Catherine Walsh https://orcid.org/0000-0001-6078-786X

References

Aikawa, Y., Cataldi, G., Yamato, Y., et al. 2021, ApJS, 257, 13
Astropy Collaboration, Price-Whelan, A. M., & Lim, P. L. 2022, ApJ, 935, 167
Bergner, J. B., Öberg, K. I., & Rajappan, M. 2019, ApJ, 874, 115
Boogert, A. C. A., Brewer, K., Brittain, A., & Emerson, K. S. 2022, ApJ, 941, 32
Booth, A., Leemker, M., van Dishoeck, E. F., et al. 2024, AJ, 167, 164
Booth, A. S., Law, C. J., Temmink, M., Leemker, M., & Macias, E. 2023, A&A, 678, A146
Booth, A. S., van der Marel, N., Leemker, M., van Dishoeck, E. F., & Ohashi, S. 2021a, A&A, 651, L6
Booth, A. S., Walsh, C., Ilee, J. D., et al. 2019, ApJL, 882, L31
Booth, A. S., Walsh, C., Terwisscha van Scheltinga, J., et al. 2021b, NatAs, 5, 684
Brown, J. M., Herczeg, G. J., Pontoppidan, K. M., & van Dishoeck, E. F. 2012, ApJ, 744, 116
Bruderer, S., van der Marel, N., van Dishoeck, E. F., & van Kempen, T. A. 2014a, A&A, 562, A26
Brunken, N. G. C., Booth, A. S., Leemker, M., et al. 2022, A&A, 659, A29
Calmonte, U., Altwegg, K., Balsiger, H., et al. 2016, MNRAS, 462, S253
Carney, M. T., Hogerheijde, M. R., Guzmán, V. V., et al. 2019, A&A, 623, A124
Carpenter, J., Brogan, C., Iono, D., & Mroczkowski, T. 2023, in Physics and Chemistry of Star Formation: The Dynamical ISM Across Time and Spatial Scales, ed. V. Ossenkopf-Okada et al. (Köln: Universitäts und Stadtbibliothekj), 304
Cazaux, S., Carrascosa, H., Muñoz Caro, G. M., et al. 2022, A&A, 657, A100
Chen, Y., van Gelder, M. L., Nazari, P., et al. 2023, A&A, 678, A137
Coletta, A., Fontani, F., Rivilla, V. M., et al. 2020, A&A, 641, A54
De Simone, M., Ceccarelli, C., Codella, C., et al. 2020, ApJL, 896, L3
Drozdovskaya, M. N., van Dishoeck, E. F., Jørgensen, J. K., et al. 2018, MNRAS, 476, 4949
Endres, C. P., Schlemmer, S., Schilke, P., Stutzki, J., & Müller, H. S. P. 2016, JMoSp, 327, 95
Ferrero, S., Zamirri, L., Ceccarelli, C., et al. 2020, ApJ, 904, 11
Follette, K. B., Grady, C. A., Swearingen, J. R., et al. 2015, ApJ, 798, 132
Fuchs, G. W., Cuppen, H. M., Ioppolo, S., et al. 2009, A&A, 505, 629
Furuya, K., Tsukagoshi, T., Qi, C., et al. 2022, ApJ, 926, 148
Gaia Collaboration, Brown, A. G. A., Vallenari, A., et al. 2018, A&A, 616, A1
Guzmán-Díaz, J., Mendigutía, I., Montesinos, B., et al. 2021, A&A, 650, A182
Hänni, N., Altwegg, K., Baklouti, D., et al. 2023, A&A, 678, A22
Harris, C. R., Millman, K. J., van der Walt, S. J., et al. 2020, Natur, 585, 357
Herbst, E., & van Dishoeck, E. F. 2009, ARA&A, 47, 427
Hunter, J. D. 2007, CSE, 9, 90
Ikeda, M., Ohishi, M., Nummelin, A., et al. 2001, ApJ, 560, 792
Kama, M., Bruderer, S., van Dishoeck, E. F., et al. 2016, A&A, 592, A83
Kluyver, T., Ragan-Kelley, B., Pérez, F., et al. 2016, in Positioning and Power in Academic Publishing: Players, Agents and Agendas, ed. F. Loizides & B. Schmidt (Amsterdam: IOS Press), 87
Laas, J. C., & Caselli, P. 2019, A&A, 624, A108
Laas, J. C., Garrod, R. T., Herbst, E., & Widicus Weaver, S. L. 2011, ApJ, 728, 71
Le Gal, R., Öberg, K. I., Teague, R., et al. 2021, ApJS, 257, 12
Leemker, M., Booth, A. S., van Dishoeck, E. F., et al. 2023, A&A, 673, A7
Ligterink, N. F. W., & Minissale, M. 2023, A&A, 676, A80
Loomis, R. A., Cleeves, L. I., Öberg, K. I., et al. 2018a, ApJ, 859, 131
Loomis, R. A., Öberg, K. I., Andrews, S. M., et al. 2018b, AJ, 155, 182
Lykke, J. M., Coutens, A., Jørgensen, J. K., et al. 2017, A&A, 597, A53
Manigand, S., Jørgensen, J. K., Calcutt, H., et al. 2020, A&A, 635, A48
Meeus, G., Montesinos, B., Mendigutía, I., et al. 2012, A&A, 544, A78
Minissale, M., Aikawa, Y., Bergin, E., et al. 2022, ESC, 6, 597
Öberg, K. I., Garrod, R. T., van Dishoeck, E. F., & Linnartz, H. 2009, A&A, 504, 891
Öberg, K. I., Guzmán, V. V., Furuya, K., et al. 2015, Natur, 520, 198
Pérez, F., & Granger, B. E. 2007, CSE, 9, 21
Pickett, H. M., Poynter, R. L., Cohen, E. A., et al. 1998, JQSRT, 60, 883
Salyk, C., Herczeg, G. J., Brown, J. M., et al. 2013, ApJ, 769, 21
Santos, J. C., Chuang, K.-J., Lamberts, T., et al. 2022, ApJL, 931, L33
Semenov, D., & Wiebe, D. 2011, ApJS, 196, 25
Temmink, M., Booth, A. S., van der Marel, N., & van Dishoeck, E. F. 2023, A&A, 675, A131
van der Marel, N., Booth, A. S., Leemker, M., van Dishoeck, E. F., & Ohashi, S. 2021a, A&A, 651, L5
van der Marel, N., Birnstiel, T., Garufi, A., et al. 2021b, AJ, 161, 33
van der Marel, N., van Dishoeck, E. F., Bruderer, S., et al. 2013, Sci, 340, 1199
van der Marel, N., van Dishoeck, E. F., Bruderer, S., et al. 2016, A&A, 585, A58
van Gelder, M. L., Tabone, B., Tabone, B., et al. 2020, A&A, 639, A87
Vioque, M., Oudmaijer, R. D., Baines, D., Mendigutía, I., & Pérez-Martínez, R. 2018, A&A, 620, A128
Walsh, C., Daley, C., Facchini, S., & Juhász, A. 2017, A&A, 607, A114
Walsh, C., Herbst, E., Nomura, H., Millar, T. J., & Weaver, S. W. 2014a, FaDi, 168, 389
Walsh, C., Juhász, A., Pinilla, P., et al. 2014b, ApJL, 791, L6
Walsh, C., Loomis, R. A., Öberg, K. I., et al. 2016, ApJL, 823, L10
Ward, M. D., Hogg, I. A., & Price, S. D. 2012, MNRAS, 425, 1264
Watanabe, N., & Kouchi, A. 2002, ApJL, 571, L173
Weaver, E., Isella, A., & Boehler, Y. 2018, ApJ, 853, 113
Wilson, T. L. 1999, RPPh, 62, 143
Wölfer, L., Facchini, S., van der Marel, N., et al. 2023, A&A, 670, A154
Yang, H., Fernández-López, M., Li, Z.-Y., et al. 2023, ApJL, 948, L2
Zhang, K., Booth, A. S., Law, C. J., et al. 2021, ApJS, 257, 5